ENVIRONMENTAL STUDIES

Dominant 100,000-year precipitation cyclicity in a late Miocene lake from northeast Tibet

Junsheng Nie,[1,2]* Carmala Garzione,[2] Qingda Su,[1] Qingsong Liu,[3,4] Rui Zhang,[1] David Heslop,[5] Cristian Necula,[6] Shihong Zhang,[7] Yougui Song,[8] Zeng Luo[1]

East Asian summer monsoon (EASM) precipitation received by northern China over the past 800 thousand years (ky) is characterized by dominant 100-ky periodicity, mainly attributed to CO_2 and Northern Hemisphere insolation–driven ice sheet forcing. We established an EASM record in the Late Miocene from lacustrine sediments in the Qaidam Basin, northern China, which appears to exhibit a dominant 100-ky periodicity similar to the EASM records during the Late Quaternary. Because evidence suggests that partial or ephemeral ice existed in the Northern Hemisphere during the Late Miocene, we attribute the 100-ky cycles to CO_2 and Southern Hemisphere insolation–driven Antarctic ice sheet forcing. This indicates a >6–million year earlier onset of the dominant 100-ky Asian monsoon and, likely, glacial and CO_2 cycles and may indicate dominant forcing of Northern Hemisphere climate by CO_2 and Southern Hemisphere ice sheets in a warm world.

INTRODUCTION

The tenet of the Milankovitch theory is that Northern Hemisphere summer insolation, controlled by Earth's orbital parameters {precession [~23 thousand years (ky)], obliquity (~41 ky), and eccentricity (~100 and ~400 ky)}, drives ice sheet size variations (*1*). However, the observed dominant 100-ky ice age cycles in paleoclimate records during the Late Quaternary challenge this theory because the insolation variations associated with Earth's orbital eccentricity are much weaker than those associated with precession and obliquity (*2*–*6*). The paleoclimate community has coined the term "the glacial 100-ky problem" to describe the perplexing dominant 100-ky climatic periodicity during the past 800 ky. Although glacial cycles during the Pliocene and the Early Quaternary do not show dominant 100-ky cycles, but instead show dominant 41-ky cycles, it is unknown whether dominant 100-ky ice sheet cycles existed during the Late Miocene when Earth was characterized by marked Antarctic ice sheet variations (*7*, *8*). This lack of knowledge of the tempo of glaciations in deep time is caused by a lack of Late Miocene ice volume records that are not conflated with deep-ocean water temperature bias (*9*).

Terrestrial ice volume variation and atmospheric CO_2 concentration covary, and they are two dominant factors controlling the East Asian summer monsoon (EASM) precipitation in northern China during the Late Quaternary (*10*–*12*). Therefore, EASM variations at orbital time scales could be potentially used to determine fluctuating patterns of the ice sheets and CO_2 during the Late Miocene. Because available Late Miocene atmospheric CO_2 records cannot yet resolve orbital time scale CO_2 variations (*13*–*15*) and the benthic oxygen isotope records include a mixed signal of ice volume and deep-ocean water temperature, often decoupled from each other (*9*), independent constraints from the Late Miocene EASM record could be crucial for determining the nature of the dominant 100-ky ice age cycles.

The northwestern limit of the modern EASM precipitation is close to the southeast margin of the Qaidam Basin (Fig. 1), and previous research has suggested that EASM precipitation likely penetrated further inland during the mid-Holocene (*12*). The Late Miocene was characterized by even warmer climate (*7*, *16*, *17*). Therefore, the Qaidam Basin is a good place to record EASM variability, in particular the migration of northwestern margin of influence of EASM precipitation, and shed new light on CO_2 and Antarctica ice sheet variations during the Late Miocene. Following the recommendation by Wang *et al.* (*18*), a stronger EASM at orbital and tectonic time scales is defined here as increased monsoon precipitation in northern China, associated with a northwestward shift of the East Asian subtropical frontal system (also called Meiyu front).

RESULTS

In the eastern part of the Qaidam Basin, Late Miocene open lacustrine sediments are exposed near the Huaitoutala (HTTL) village (*19*). The lack of positive correlation between oxygen and carbon isotopic compositions of bulk carbonate supports the sedimentary interpretation of an open lacustrine depositional environment for these strata (fig. S1). We performed paleomagnetic sampling of this section to establish a high-resolution age model (Fig. 2) and then reconstructed variability of the EASM during this time interval on the basis of a recently developed magnetic monsoon proxy (*20*) that is sensitive to monsoon precipitation, but not to temperature (Fig. 3).

Age model

A preliminary age model of the section that is based on 2- to 5-m resolution magnetostratigraphy and multiple fauna layers was established by Fang *et al.* (*21*). Our higher-resolution paleomagnetic resampling and analysis (0.5 to 1 m) of the middle portion of the section allowed us to find all reversed polarities within the previous age model framework, improving the robustness of the age model (Fig. 2). For example, C3Bn, C3Br.1n, C4Ar.2n, and C5n.1n were not recognized in the age model of Fang *et al.* (*21*) (Fig. 2). In addition, the age model by Fang *et al.* (*21*) only recognized a portion of C3Br.2n and C4n.1n, resulting in a longer C3Br.2n than C4n.1n, opposite to the

[1]Key Laboratory of Western China's Environmental System (Ministry of Education), College of Earth and Environmental Sciences, Lanzhou University, Lanzhou, Gansu 730000, China. [2]Department of Earth and Environmental Sciences, University of Rochester, Rochester, NY 14627, USA. [3]Department of Marine Science and Technology, South University of Science and Technology of China, Shenzhen 518055, China. [4]Laboratory for Marine Geology, National Oceanography Laboratory, Qingdao 266061, China. [5]Research School of Earth Sciences, Australian National University, Canberra, Australian Capital Territory 0200, Australia. [6]Faculty of Physics, Paleomagnetic Laboratory, University of Bucharest, Nicolae Balcescu, Sector 1, 010041 Bucharest, Romania. [7]State Key Laboratory of Biogeology and Environmental Geology, China University of Geosciences, Beijing 100083, China. [8]State Key Laboratory of Loess and Quaternary Geology, Institute of Earth Environment, Chinese Academy of Sciences, P.O. Box 17, Xi'an 710075, China.
*Corresponding author. Email: jnie@lzu.edu.cn

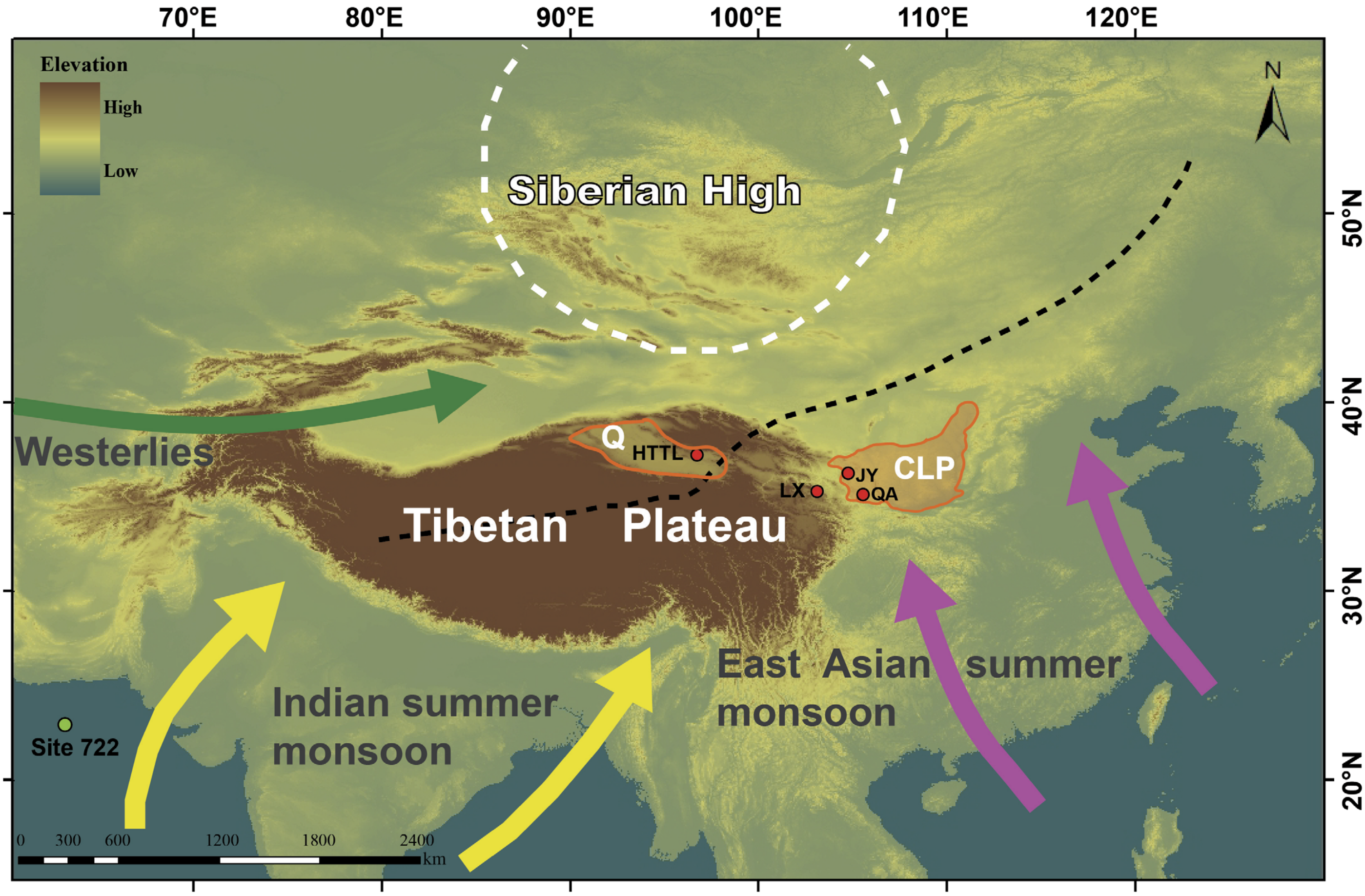

Fig. 1. Map of the study sites and atmospheric circulation pattern. Black dashed line depicts the Asian summer monsoon fringes at present (*84*). The white dashed circle represents the Siberian High in January. HTTL, Huaitoutala; LX, Linxia; JY, Jingyuan; QA, Qinan; Q, Qaidam Basin; CLP, Chinese Loess Plateau.

pattern in the geomagnetic polarity time scale (GPTS). All of these deficiencies are now fixed in our higher-resolution results. This greater age model precision is essential for spectral analysis. We found 12 normal polarities (N1 to N12), which we correlate to the 12 normal polarities between 10 and 6 Ma (million years ago) in the GPTS (*22*). We established the age model by piecewise linear interpolation using the reversal ages (table S1).

The northern China precipitation record

The new magnetic monsoon proxy χ_{fd}/HIRM (frequency-dependent magnetic susceptibility/hard isothermal remanent magnetization) reflects the ratio of fine nanometer-scale ferrimagnets (magnetite and maghemite; measured by χ_{fd}) over hematite (measured by HIRM) (see Materials and Methods). Magnetic remanence unmixing analysis reveals the common existence of two types of magnetic minerals with coercivity peaks of 26 and 330 mT, which we infer correspond to fine magnetite/maghemite and hematite, respectively (fig. S2). These fine magnetic minerals are produced during weathering processes, but production of hematite requires less precipitation in comparison with fine ferrimagnetic grains (*23*, *24*). Thus, high χ_{fd}/HIRM indicates strong EASM precipitation and more intense diagenetic weathering.

The χ_{fd}/HIRM record suggests intensified EASM precipitation during ~8.5 to 7 Ma (Fig. 4D and data set S1). This can be further verified by both the chlorite/(goethite + hematite) ratio and the halite content data from the same section (see Materials and Methods and fig. S3). Chlorite is a product of physical erosion, whereas goethite and hematite are largely produced by chemical weathering (*25*). Thus, their ratio can reflect weathering intensity (*25*). Halite represents later-stage evaporation of a lake (*26*); thus, here, higher halite content is interpreted to indicate a drier climate. These proxy records are all consistent with a phase of wet climate during 8.5 to 7 Ma (Fig. 4, E and F, and data set S1).

Other East Asia archives also record this phase of wetting. In Linxia (*27*), the oxygen isotope values of lacustrine sediments decreased after ~8.5 Ma, interpreted as wetter climate (Fig. 4C). On the western Chinese Loess Plateau (CLP) (*28*), Qinan magnetic susceptibility (χ) increased during ~8.5 to 7.2 My (Fig. 4B), indicating wetter climate. Thus, there is consistency between independent methods and locations in East Asia for greater precipitation approximately coeval with the Qaidam record.

DISCUSSION

Million-year time scale variations of EASM

EASM precipitation pattern in China is determined mainly by the jet stream's interaction with the Tibetan Plateau (mechanical role) (*29*) and by heating of the plateau (thermal role) (*30*, *31*). The Tibetan Plateau interacts with the jet stream to steer the subtropical frontal system east of the Tibetan Plateau, promoting precipitation in China (*29*). Intensified heating associated with a high plateau can amplify the low-pressure system

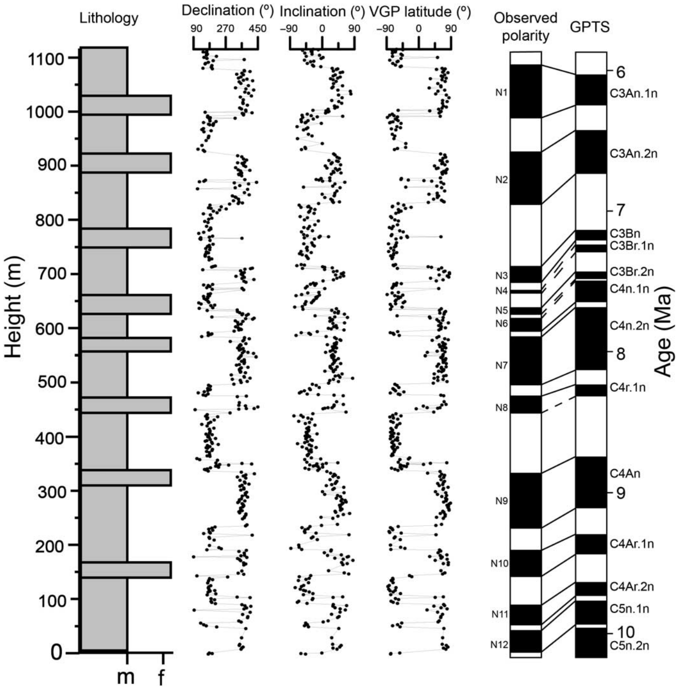

Fig. 2. Age model and lithology (*19*) of Late Miocene HTTL section in the Qaidam Basin. C3Br.1n and the reversed interval between C3Br.2n and C4n.1n are each constrained by a single data point. The bottom boundary of C4r.1n in the observed polarity has multiple possibilities. Therefore, these five reversal ages (which correspond to the dashed lines) are not used to establish the age model. VGP, virtual geomagnetic polarity (*22*); m, mudstone; f, fine sandstone.

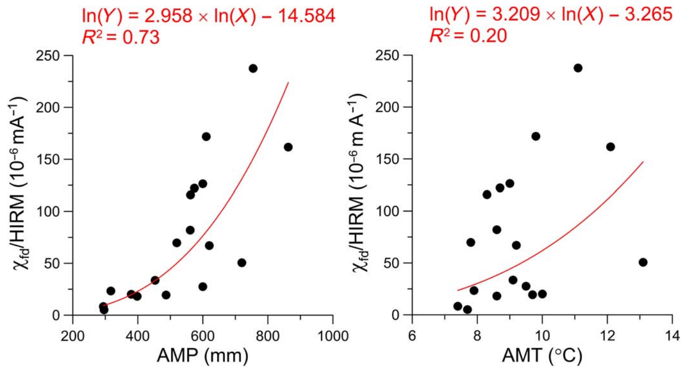

Fig. 3. χ_{fd}/HIRM versus annual mean precipitation and temperature for surface soil samples across the CLP. The annual mean temperature (AMT) and the annual mean precipitation (AMP) data are from meteorological stations on the CLP. The sample sites are the same as those in the study by Nie *et al.* (*85*).

on the Tibetan Plateau, amplifying sea-land pressure contrast and causing additional precipitation in China (*30*, *31*). When the (northern) Tibetan Plateau is low, these effects are weakened, resulting in decreased EASM precipitation (*31*, *32*). Therefore, upward and/or outward growth of the marginal portions of the Tibetan Plateau will result in penetration further inland of the EASM precipitation, as was recently demonstrated in model simulations (*33*). Sedimentological and thermochronology evidence reveals that the northeastern Tibetan Plateau experienced a phase of upward and/or outward growth during the Late Miocene (*34*, *35*). For example, low-temperature thermochronology data reveal that rapid exhumation occurred in the Liupan Shan (*36*) and the north Qilian Shan (*37*) areas, and sedimentary accumulation rates (*38*) and provenance data (*39*) in the Guide Basin reveal rapid exhumation of the Laji Shan during the Late Miocene. Therefore, we predict a coeval increase in inland Asia precipitation if the northern margin of the northeastern Tibetan Plateau rapidly propagated into inland Asia in the Late Miocene. However, this inference is in contradiction with the widely held idea of Late Miocene Asian drying, which is based on increased dust accumulation in the North Pacific Ocean (*40*) and the onset of loess accumulation on the central CLP around 8 Ma (*41*, *42*). Recent studies reveal that CLP dust does not necessarily come from deserts and that increased dust accumulation does not necessarily indicate inland Asian aridification (*43*–*46*). This is because tectonic deformation can produce dust for wind to entrain and transport downwind (*44*, *47*). Specifically, the older loess (~8 Ma) on the central CLP has a relatively large zircon grain size compared to the typical loess, which has been attributed to tectonic deformation–produced dust associated with growth of the Liupan Mountains and wind erosion in the Qaidam Basin (*44*, *46*). Furthermore, dry riverbeds have recently been recognized as important dust sources for the CLP and, by inference, for the downwind North Pacific Ocean (*43*, *45*, *46*).

The records we compile and present here demonstrate that, contrary to common thinking, northern China has become wetter since ~8.5 Ma. The South Asian records also reveal a phase of wetting during ~8.5 to 7 Ma. The C_4 plant expansion trend, initiating from at least 10 Ma, shows a reversal pattern (Fig. 4A) as recorded by leaf wax carbon isotope in the Indian Ocean sediments (*48*); higher plant leaf waxes mainly came from regions around Pakistan, Iran, Afghanistan, and the Arabian Peninsula. Together, the approximate synchroneity in both the East Asian and the South Asian records suggests that the growth of northeastern Tibet during the Late Miocene might have had significant effects on climate both north and south of the Tibetan Plateau (Fig. 1). On the other hand, if the entire plateau or additional margins of the Tibetan Plateau experienced a phase of rapid outward and upward growth at ~8.5 Ma, as proposed by some researchers (*49*), this may explain the synchronous climatic wetting both north and south of the Tibetan Plateau. Regardless of the scale of the growth of the Tibetan Plateau (northeastern growth versus upward growth), it is noteworthy that oxygen isotopic compositions of benthic foraminifera at Ocean Drilling Program (ODP) site 982 (*50*) reveal a phase of climatic cooling/ice sheet growth at ~8.5 Ma (Fig. 4H), suggesting that atmospheric CO_2 concentrations also declined. It is plausible that Late Miocene expansion of the Tibetan Plateau has played a role in global climate cooling, perhaps through silicate weathering (*51*) and increased carbon burial (*52*).

Ice-rafted debris started to reach ODP site 918, North Atlantic Ocean, starting from ~7 Ma (*53*), indicating that ice sheets in Greenland had expanded to the sea by then. We attribute weakening of the EASM after 7 Ma to the initiation of Northern Hemisphere glaciations (*7*) and decreased Northern Hemisphere sea surface temperature (*17*, *48*, *54*), which caused a southward shift of the dry limb of the Hadley circulation.

Although we outline a plausible mechanism for million-year time scale EASM precipitation variations during the Late Miocene, other possibilities exist. For example, some studies (*55*–*58*) suggest Eocene establishing of the northern Tibetan Plateau. If this is the case, the reason for the observed million-year time scale EASM variations needs further research. Furthermore, some evidence suggests that Northern Hemisphere land has at least ephemeral ice sheets before 7 Ma (*59*, *60*). However, the sensitivity of the EASM to small-scale Northern Hemisphere ice sheet size variation is unknown, stimulating further research.

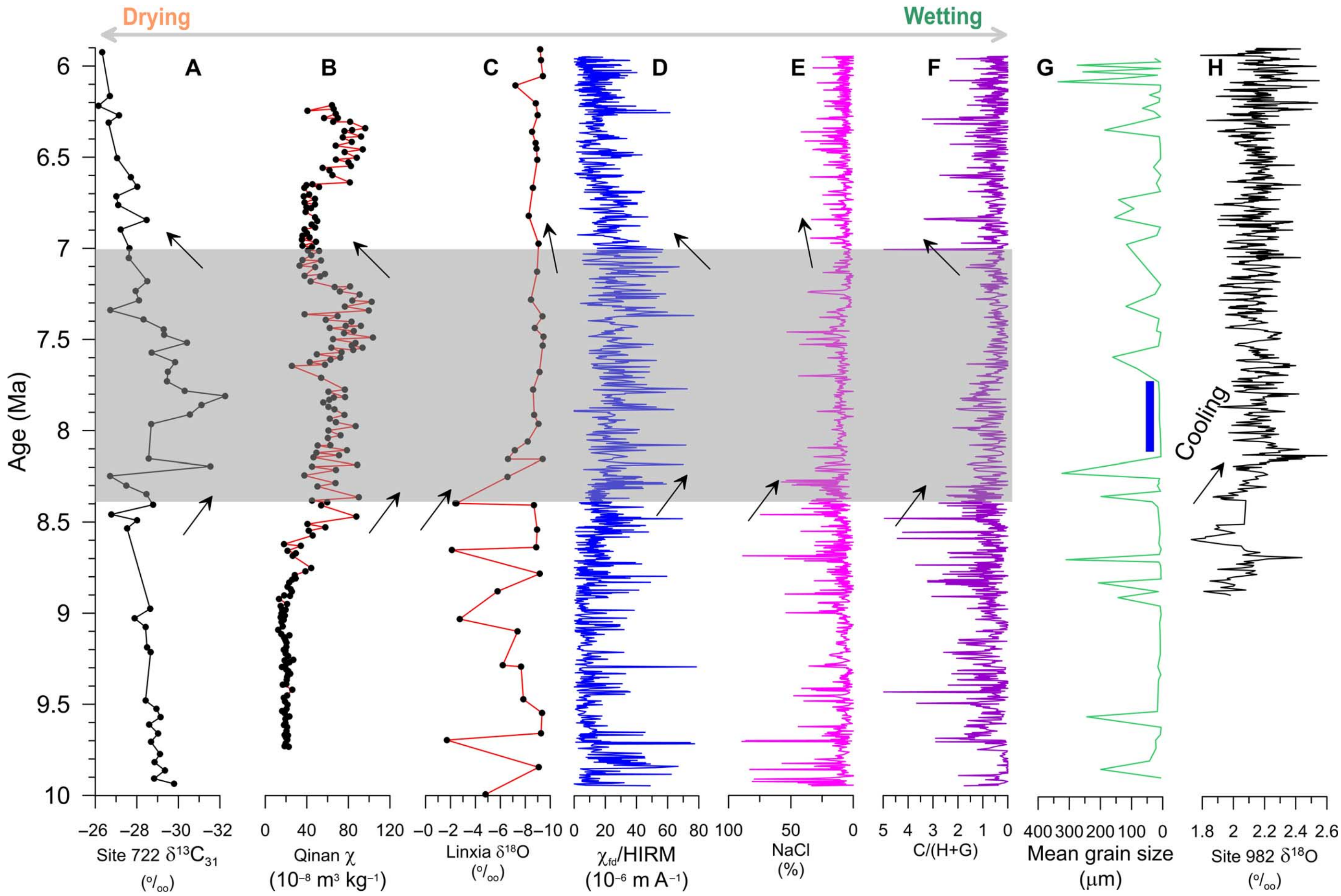

Fig. 4. Paleoenvironmental records during the Late Miocene. (**A**) Ocean Drilling Program (ODP) site 722 *n*-alkane C_{31} carbon isotope record (*48*). (**B**) Qinan loess magnetic susceptibility (χ) record (*86*). (**C**) Linxia lacustrine sediment oxygen isotope record (*27*). (**D** to **G**) Qaidam Basin HTTL section χ_{fd}/HIRM, halite content, chlorite/(hematite + goethite) [C/(H+G)] ratio, and mean grain size record. (**H**) Benthic oxygen isotope record from ODP Site 982, North Atlantic Ocean (*50*). We did not include several negative χ_{fd}/HIRM and unrealistically high χ_{fd}/HIRM and C/(H+G) values from the Qaidam records. To promote readability, wetting corresponds to the right-hand direction for the Asian monsoon records. The blue bar in (G) shows the interval that has relatively constant grain size without flooding events for over 400 ky after 8.5 Ma.

Orbital time scale variations of monsoon and ice volume

The χ_{fd}/HIRM record shows cyclicity, especially between 8.5 and 7 Ma when the record shows higher values than before and after. Spectral analysis of the environmental magnetic data reveals that 100-ky eccentricity cycles have the strongest signal (Figs. 4 and 5). Model simulation suggests that Tibetan uplift can amplify the EASM's sensitivity to insolation forcing because of its thermal role on precipitation (*31*, *32*). Several lines of geological evidence (*36*–*39*) suggest a phase of northeastward or upward growth of the Tibetan Plateau during the Late Miocene, which can explain the enlarged climatic fluctuation amplitude observed here (Fig. 4). The HTTL grain size record (Fig. 4G) shows that during ~8.18 to 7.78 Ma, there is a 400-ky-long interval where the sediment grain size is relatively uniform, indicating non–flood-transported coarse grains, but in the other intervals after 8.5 Ma, grain size pulses are associated with periodic flooding. Therefore, we compared the χ_{fd}/HIRM record during 8.18 to 7.78 Ma with the loess χ record on the northwestern CLP during the past ~400 ky (*10*). The two records show marked similarities in both time and frequency domains, with the 100-ky cycle as the dominant period (Fig. 6). Similar to the Late Quaternary, the Late Miocene 100-ky cycles also consist of bundling of several precession and/or obliquity cycles (*6*, *61*, *62*), suggesting similar forcing mechanisms.

These precession and obliquity signals are not as clear in the central CLP record (*63*) as those in the northwestern CLP record (Fig. 6, C and F). We attribute this to low sediment accumulation rate and precipitation-driven postdepositional alteration of loess deposited in situ and the underlying loess on the central CLP, which caused signal smearing (*64*). This explanation is supported by sedimentological observation. For example, paleosol S1 (with a depositional age of ~0.1 Ma; Fig. 6) consists of three distinct dark-colored subpaleosol units interlayered with two light-colored subloess units for the northwestern CLP, but for the central CLP site, S1 is a dark layer without subloess layers (*65*). Thus, to accurately record variations of the EASM, sites with high sedimentation rates and little postdepositional alteration are preferred. The HTTL section, which is next to the northeastern edge of the EASM (Fig. 1), with about four times higher sedimentation rate during 10 to 6 Ma than the Quaternary loess from the central CLP, should provide a more reliable EASM intensity signal during the Late Miocene.

In theory, the 100-ky cycles would be intensified if the climatic record shows a muted response to the cold phase of insolation forcing; however, such a response will still show dominant variability at the 23-ky band (fig. S4). Our sampling resolution is ~3.6 ky for the interval from 8.5 to 7 Ma, which is high enough to resolve the 23-ky signal. The observation

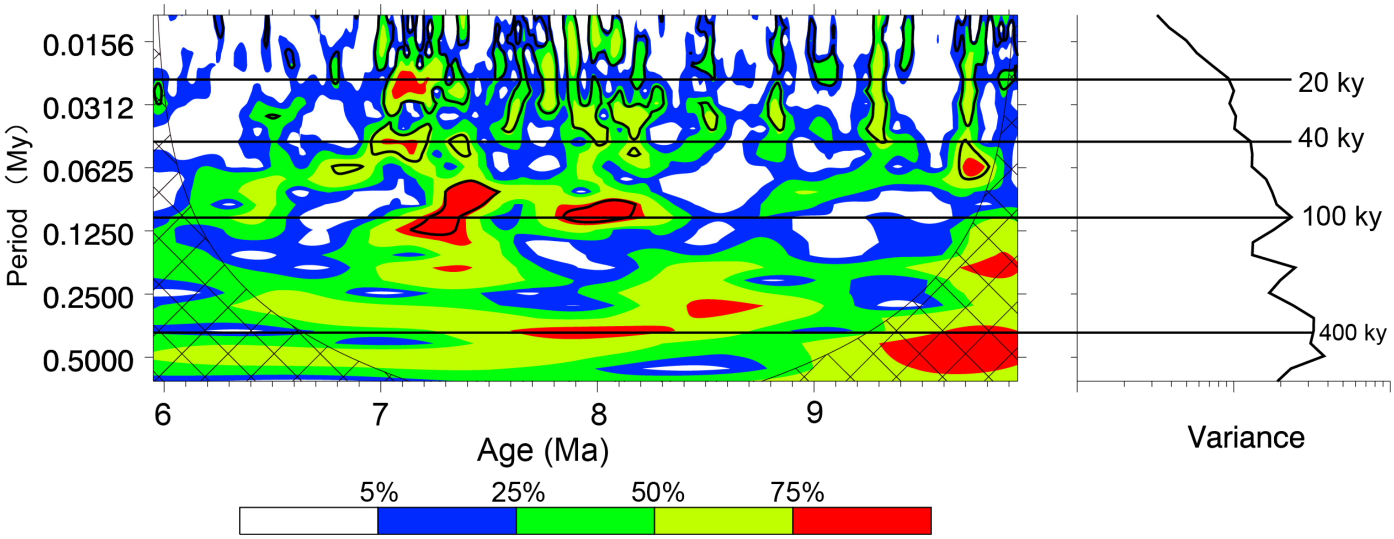

Fig. 5. The wavelet transform (*87*) (left) and the power spectrum (right) of the χ_{fd}/HIRM record from the Qaidam Basin. The color scale indicates power, which is scaled to percent total power, and the hatched areas illustrate the cone of influence and, hence, the edge effects of the transform. We note that warm color indicates larger power. The 400-, 100-, 40-, and 20-ky periodicities are labeled and indicated by the straight black lines. The black contour is the 20% significance level, using a red noise background spectrum.

that the 23-ky signal is much weaker than the 100-ky signal suggests that the EASM's muted response to the cold phase of insolation forcing is not the main reason for the observed dominant 100-ky cycles.

Because ephemeral ice existed in the Northern Hemisphere before 7 Ma, as is suggested by the ice rafting record of southeast Greenland (*53*), the dominant 100-ky cycles in our monsoon record could be attributed to Southern Hemisphere insolation–driven Antarctic ice sheet forcing. There are several ways that Antarctica ice sheet size variations could affect the monsoon. First, sea level variations associated with Antarctica ice sheet size variations during the Late Miocene would have caused periodic advance and retreat of the EASM northeastern edge, as observed in the Late Quaternary (*10*, *12*). Second, tropical Pacific Ocean water evaporation will decrease during lower sea surface temperatures associated with colder glacial climate, which would cause additional retreat of the extent of EASM precipitation. On the basis of estimates from the South China Sea, moisture evaporation associated with surface seawater cooling decreased by $^1/_8$ to $^1/_4$ during the last glacial maximum in comparison with current China annual precipitation (*66*), which can cause a significant decrease of the EASM precipitation, especially near its northwestern extent. Third, research suggests that Antarctica ice sheet size variation was an important driving force affecting the orbital time scale Asian summer monsoon intensity via changing cross-equatorial pressure gradient and amount of latent heat release during the Pleistocene (*67*, *68*).

During 7 to 1 Ma, ice sheet expansion and shrinking occurred in both hemispheres forced by local insolation, resulting in strengthened 41-ky obliquity cycles (*69*). In the Late Quaternary after ~1 Ma, the Antarctic ice sheets grew to be marine-based, and from then on, the Antarctic ice sheets ceased being controlled by local insolation but was instead controlled by eustatic sea level (*69*). When the Northern Hemisphere has larger ice sheets and sea level is low, Antarctic ice sheets also expanded over continental shelf area exposed by sea level fall; when sea level is high during interglacials, Antarctic ice sheets lose ice by rafting and calving of the margins of the ice sheets. Thus, global ice volume variations are mainly caused by ice sheet expansion and shrinking in the Northern Hemisphere after ~1 Ma (*69*), resulting in the reappearance of the dominant 100-ky cycles.

The published benthic oxygen isotope records during the Oligocene and the Early Miocene (*7*, *70*) show strong 100-ky cycles, supporting the inference that the Antarctica ice sheet was fluctuating at a dominant 100-ky periodicity before the formation of Northern Hemisphere ice sheets after 7 Ma. Furthermore, a recent study (*71*) separated Antarctica ice volume variations from the Late Oligocene–Early Miocene benthic oxygen isotope record on the basis of inverse modeling, and the results show that the Antarctica ice sheets were dominated by 100-ky pacing, particularly during the termination phases of the major Antarctic glaciations, further supporting our inference.

Although this mechanism is plausible, we cannot exclude the fact that CO_2 is an important forcing mechanism of EASM variability at orbital time scales. It could well be that CO_2 covaried with Antarctica ice sheet fluctuation at orbital time scales, similar to the condition for the past 800 ky between CO_2 and Northern Hemisphere ice sheets. Unfortunately, available CO_2 records (*13*, *72*) do not yet have the resolution to resolve orbital time scale variability.

In summary, we reveal that the northern China precipitation was fluctuating at a dominant 100-ky pace during the Late Miocene. Therefore, although the dominant 100-ky cycles during the Late Quaternary are considered anomalous by the paleoclimate community (*2*, *3*), they appear to have been the dominant cycle at least 6 to 7 My earlier in the EASM and, likely, ice sheet records. Considering the recent discovery of the Eocene onset of the EASM (*73*–*75*) and strong pre-Miocene 100-ky cycles in the Antarctica ice sheet (*7*, *70*) and Asian aridification records (*76*), it is likely that the dominant 100-ky eccentricity cycles exist in the pre-Miocene EASM records when data with enough resolution are available for this older interval.

If our model is correct, under future warming scenarios where the Greenland Ice Sheet markedly shrinks and the Antarctica ice sheet is land-based again, the 100-ky ice age and EASM cycles experienced during the past 800 ky will continue because of ice sheet expansion and shrinking in Antarctica caused by Southern Hemisphere summer insolation

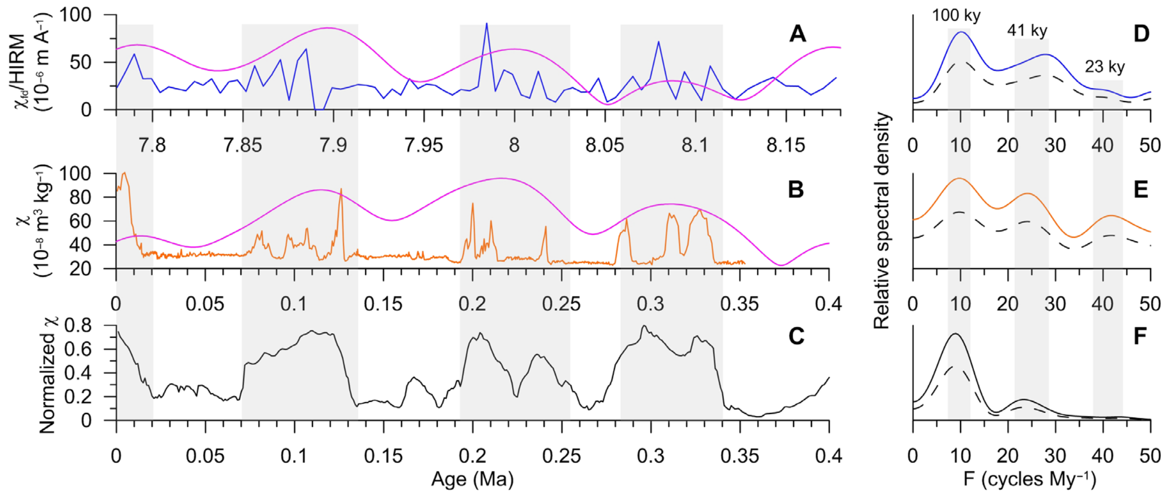

Fig. 6. A comparison of the EASM variations during the Late Miocene and the Late Quaternary for a time period of ~400 ky. (**A**) The χ_{fd}/HIRM record from the Qaidam Basin during 8.18 to 7.78 Ma. (**B**) The χ record from Jingyuan in the northwestern CLP during the past ~400 ky (*10*). (**C**) The normalized χ record from the central CLP during the past ~400 ky (*63*). (**D** to **F**) The power spectrum of (A) to (C) (solid lines) and the lower limit of their 80% significance interval (dashed lines). The power spectrum was generated using the AnalySeries 2.0.4 software (*88*). For comparison, the eccentricity data (pink curves; higher value is upward) (*89*) during 8.18 to 7.78 Ma and 0.4 to 0 Ma are also shown in (A) and (B), respectively

variations, which is opposite to Northern Hemisphere summer insolation variations.

MATERIALS AND METHODS

Paleomagnetism dating

Oriented cylindrical paleomagnetic samples were taken at intervals of 1 m from the middle portion of the HTTL section in August 2011 using a portable gasoline-powered drill, and loose samples were also taken from the same stratigraphic level for paleoenvironmental reconstruction purpose. This portion corresponds to the upper Shang Youshanshan and lower Shizigou formations, deposited in an open lacustrine environment (fig. S1) (*19*). The oriented samples were cut into a height of ~2 cm in the laboratory and thermally demagnetized and analyzed in the Paleomagnetism Laboratory in the Institute of Geology and Geophysics, Chinese Academy of Sciences, and in the Ministry of Education Key Laboratory of Western China's Environmental Systems, Lanzhou University, China. Pilot samples and previous studies (*21*) show that viscous remanence is removed before 350°C and that hematite is an important remanence carrier. Therefore, we performed thermal demagnetization at temperatures 350°, 450°, 500°, 550°, 570°, 580°, 610°, 630°, 650°, and 670°C for the rest of the samples.

Environmental magnetism

Loose samples were crushed and packed in a box of 2 × 2 × 2 cm, and magnetic susceptibility (χ) was measured at 976 and 15,616 Hz, respectively, with Multi-Function Kappabridge in the Paleomagnetism Laboratory of the China University of Geosciences, Beijing, China. χ_{fd} is calculated as the χ difference measured at 976 and 15,616 Hz. Isothermal remanent magnetism (IRM) was imparted first at 1 T and then at –0.1 and –0.3 T. The HIRM (or hard IRM) is calculated as the sum of IRM_{1T} and $IRM_{-0.3T}$ divided by 2. The *L* ratio is calculated as HIRM/[0.5 × (IRM_{1T} + $IRM_{-0.1T}$)] (*77*). If HIRM and *L* ratio are not correlated with each other, HIRM can be considered as a valid proxy for hematite content (*77*). Figure S5 shows that HIRM and *L* ratio are not correlated, supporting that HIRM can be used to indicate hematite content in this case.

Samples (104) were ground into powder before backfield measurements were performed on a PMC vibrating sample magnetometer (MicroMag 3900) at the Paleomagnetic Laboratory, University of Bucharest, Romania. Samples were first saturated at 1 T, and then the field was reversed and nonlinearly incremented until −1 T in 30 steps. To interpret backfield demagnetization curves, we used here the unmixing algorithm of Heslop and Dillon (*78*), as in the loess–red clay samples in the CLP (*79*). This method does not require prior knowledge of different components, but instead isolate different components based on an assemblage of measured samples. The estimation of the number of end members to be included in the unmixing model is based on the calculation of the coefficient of determination, R^2, versus the number of end members through the principal component analysis.

X-ray diffraction patterns

The analyses were carried out on crushed samples using a Rigaku D/Max-2400 diffractometer with a Cu Kα (λ = 1.54056 Å) radiation operating at 40-kV voltage and 60-mA current in the School of Physical Science and Technology, Lanzhou University. The x-ray diffraction patterns were obtained at a scanning rate of 15°/min, with a step width in the 2θ scan of 0.02° in the range 3° to 80°. The intensity of each mineral was estimated from peak height.

Diffuse reflectance spectroscopy

Diffuse reflectance spectroscopy across the entire wavelength spectrum of visible light (400 to 700 nm) in a 0.5-nm step was performed using a Peking PUXI TU-1901 spectrophotometer equipped with a $BaSO_4$-coated integrating sphere that is 58 mm in diameter (IS19-1, Purkinje General). Samples were previously powdered and pressed by hand into the circular holes of sample holders (thickness, 2.5 mm) at a pressure >500 kPa. The resulting mounts were self-supporting, thus allowing the holders to be vertically placed without the powder falling into the sphere. Following the measurements, the signals were unmixed using the nonnegative matrix factorization method (*80*). A three-component unmixing is the simplest model that provides a high-quality fit to the measured data and separates the unweathered mineral chlorite from the weathered minerals hematite and goethite (fig. S3). Then, a revised R_{CAT} parameter (*25*) was calculated as chlorite/(hematite + goethite).

Grain size

The grain size of the powered samples was analyzed using a Malvern Mastersizer 2000 particle size analyzer, within the range of 2000 to 0.01 μm. Before analysis, samples were pretreated with hot hydrogen peroxide to remove organic matter and with hydrochloric acid to remove carbonate, following the standard procedure at the Lanzhou University.

Monsoon proxy explanation

The new magnetic monsoon proxy reflects the ratio of fine (nanometer-scale) ferrimagnetic (measured by frequency-dependant susceptibility, χ_{fd}) over hematite (measured by HIRM) grains produced during sediment erosion from source regions and transport until they were deposited within the lake. This process is rapid in the northeastern Qaidam basin and was caused by the active tectonics of the northeastern Tibetan Plateau during the Late Miocene. Provenance analysis (*81*) demonstrates that the sediment source for the studied section had always been the Qilian Shan and Nanshan Mountains to the northeast since the Early Miocene, which is within some tens of kilometers. Therefore, parent materials are relatively uniform. Previous works (*20*, *23*, *82*) reveal that diagenetic modification to rocks will produce nanometer-scale ferrimagnetic (maghemite and magnetite) and antiferrimagnetic (hematite and goethite) minerals, and production of ferrimagnetic materials requires more precipitation than hematite. A previous research (*20*) and our own calibration (Fig. 3) using surface soils on the CLP also reveal that their ratio is not sensitive to temperature variations. By assuming that there was no dissolution for magnetic materials after they were deposited in lake, their ratio can be used as a proxy for EASM intensity. Dissolution of magnetic minerals usually occurs under reduced conditions where oxygen is limited. However, open lacustrine settings (as suggested by scattered stable oxygen and carbon correlation plot; fig. S1) indicate that oxygen was not likely limited. The IRM unmixing result (fig. S2) provides direct support to this inference. The ubiquitous existence of the 26- and 330-mT component indicates that fine maghemite/magnetite and hematite grains did not dissolve (*83*). The 88-mT component corresponds to partially oxidized coarse magnetite grains (*79*), again indicating a generally oxidizing depositional environment. The consistency between the magnetic precipitation record with the evaporite mineralogy and chloride/(goethite + hematite) records (Fig. 4) further demonstrates that the magnetic precipitation record in the Qaidam Basin reliably records erosion and runoff, which we interpret as an EASM intensity signal during the Late Miocene.

SUPPLEMENTARY MATERIALS

Supplementary material for this article is available at http://advances.sciencemag.org/cgi/content/full/3/3/e1600762/DC1

fig. S1. A comparison of oxygen and carbon isotope data of the HTTL section.

fig. S2. Unmixing of backfield IRM curves of the HTTL samples.

fig. S3. The smoothed end-member reflectance spectra (left) and its first derivative spectra (right) for the HTTL samples.

fig. S4. A comparison of power spectrum of full (lower) and truncated (upper) insolation for July at 35°N (*73*).

fig. S5. A comparison of HIRM and *L* ratio for the HTTL samples.

table S1. Age tie points used to establish the age model for the HTTL section.

data set S1. HTTL section paleoclimatic data in Fig. 4.

REFERENCES AND NOTES

1. M. K. Milankovitch, Kanon der erdbestrahlung und seine anwendung anf daseiszeitenproblem. *Serb. Acad. Beorg. Spec. Publ.* **132** (1941).
2. J. Imbrie, A. Berger, E. A. Boyle, S. C. Clemens, A. Duffy, W. R. Howard, G. Kukla, J. Kutzbach, D. G. Martinson, A. McIntyre, A. C. Mix, B. Molfino, J. J. Morley, L. C. Peterson, N. G. Pisias, W. L. Prell, M. E. Raymo, N. J. Shackleton, J. R. Toggweiler, On the structure and origin of major glaciation cycles 2. The 100,000-year cycle. *Paleoceanography* **8**, 699–735 (1993).
3. L. E. Lisiecki, M. E. Raymo, Plio–Pleistocene climate evolution: Trends and transitions in glacial cycle dynamics. *Quat. Sci. Rev.* **26**, 56–69 (2007).
4. J. D. Hays, J. Imbrie, N. J. Shackleton, Variations in the Earth's orbit: Pacemaker of the ice ages. *Science* **194**, 1121–1132 (1976).
5. M. E. Raymo, Glacial Puzzles. *Science* **281**, 1467–1468 (1998).
6. Z. Liu, T. D. Herbert, High-latitude influence on the eastern equatorial Pacific climate in the early Pleistocene epoch. *Nature* **427**, 720–723 (2004).
7. J. Zachos, M. Pagani, L. Sloan, E. Thomas, K. Billups, Trends, rhythms, and aberrations in global climate 65 Ma to present. *Science* **292**, 686–693 (2001).
8. J. C. Zachos, G. R. Dickens, R. E. Zeebe, An early Cenozoic perspective on greenhouse warming and carbon-cycle dynamics. *Nature* **451**, 279–283 (2008).
9. E. J. Rohling, G. L. Foster, K. M. Grant, G. Marino, A. P. Roberts, M. E. Tamisiea, F. Williams, Sea-level and deep-sea-temperature variability over the past 5.3 million years. *Nature* **508**, 477–482 (2014).
10. Y. Sun, J. Kutzbach, Z. An, S. Clemens, Z. Liu, W. Liu, X. Liu, Z. Shi, W. Zheng, L. Liang, Y. Yan, Y. Li, Astronomical and glacial forcing of East Asian summer monsoon variability. *Quat. Sci. Rev.* **115**, 132–142 (2015).
11. F. Heller, T. S. Liu, Magnetostratigraphical dating of loess deposits in China. *Nature* **300**, 431–433 (1982).
12. T. Liu, Z. Ding, Chinese loess and the paleomonsoon. *Annu. Rev. Earth Planet. Sci.* **26**, 111–145 (1998).
13. D. J. Beerling, D. L. Royer, Convergent cenozoic CO_2 history. *Nat. Geosci.* **4**, 418–420 (2011).
14. A. K. Tripati, C. D. Roberts, R. A. Eagle, Coupling of CO_2 and ice sheet stability over
major climate transitions of the last 20 million years. *Science* **326**, 1394–1397 (2009).
15. M. Pagani, Z. H. Liu, J. LaRiviere, A. C. Ravelo, High Earth-system climate sensitivity determined from Pliocene carbon dioxide concentrations. *Nat. Geosci.* **3**, 27–30 (2010).
16. B. H. Passey, L. K. Ayliffe, A. Kaakinen, Z. Zhang, J. T. Eronen, Y. Zhu, L. Zhou, T. E. Cerling, M. Fortelius, Strengthened East Asian summer monsoons during a period of high-latitude warmth? Isotopic evidence from Mio-Pliocene fossil mammals and soil carbonates from northern China. *Earth Planet. Sci. Lett.* **277**, 443–452 (2009).
17. J. P. LaRiviere, C. Ravelo, A. Crimmins, P. S. Dekens, H. L. Ford, M. Lyle, M. W. Wara, Late Miocene decoupling of oceanic warmth and atmospheric carbon dioxide forcing. *Nature* **486**, 97–100 (2012).
18. B. Wang, Z. Wu, J. Li, J. Liu, C.-P. Chang, Y. Ding, G. Wu, How to measure the strength of the East Asian summer monsoon. *J. Climate* **21**, 4449–4463 (2008).
19. G. Zhuang, J. K. Hourigan, B. D. Ritts, M. L. Kent-Corson, Cenozoic multiple-phase tectonic evolution of the northern Tibetan Plateau: Constraints from sedimentary records from Qaidam basin, Hexi Corridor, and Subei basin, northwest China. *Am. J. Sci.* **311**, 116–152 (2011).
20. Z. Liu, Q. Liu, J. Torrent, V. Barrón, P. Hu, Testing the magnetic proxy χ_{FD}/HIRM for quantifying paleoprecipitation in modern soil profiles from Shaanxi Province, China. *Glob. Planet. Change* **110**, 368–378 (2013).
21. X. Fang, W. Zhang, Q. Meng, J. Gao, X. Wang, J. King, C. Song, S. Dai, Y. Miao, High resolution magnetostratigraphy of the Neogene Huaitoutala section in the eastern Qaidam Basin on the NE Tibetan Plateau, Qinghai Province, China and its implication on tectonic uplift of the NE Tibetan Plateau. *Earth Planet. Sci. Lett.* **258**, 293–306 (2007).
22. F. M. Gradstein, J. G. Ogg, M. Schmitz, G. Ogg, Eds., *The Geologic Time Scale 2012* (Elsevier, 2012).
23. U. Schwertmann, R. M. Taylor, in *Minerals in Soil Environments,* J. B. Dixon, S. B. Weed, Eds. (Soil Science Society of America Book Series, Soil Science Society of America, ed. 2, 1987), pp. 379–438.
24. W. L. Balsam, B. B. Ellwood, J. Ji, E. R. Williams, X. Long, A. El Hassani, Magnetic susceptibility as a proxy for rainfall: Worldwide data from tropical and temperate climate. *Quat. Sci. Rev.* **30**, 2732–2744 (2011).

25. P. D. Clift, K. V. Hodges, D. Heslop, R. Hannigan, H. Van Long, G. Calves, Correlation of Himalayan exhumation rates and Asian monsoon intensity. *Nat. Geosci.* **1**, 875–880 (2008).
26. S. Boggs, *Principles of Sedimentology and Stratigraphy* (Pearson Prentice Hall, 2006).
27. M. Fan, D. L. Dettman, C. Song, X. Fang, C. N. Garzione, Climatic variation in the Linxia basin, NE Tibetan Plateau, from 13.1 to 4.3 Ma: The stable isotope record. *Palaeogeogr. Palaeoclimatol. Palaeoecol.* **247**, 313–328 (2007).
28. Q. Z. Hao, F. Oldfield, J. Bloemendal, Z. T. Guo, The magnetic properties of loess and paleosol samples from the Chinese Loess Plateau spanning the last 22 million years. *Palaeogeogr. Palaeoclimatol. Palaeoecol.* **260**, 389–404 (2008).
29. P. Molnar, W. R. Boos, D. S. Battisti, Orographic controls on climate and paleoclimate of Asia: Thermal and mechanical roles for the Tibetan Plateau. *Annu. Rev. Earth Planet. Sci.* **38**, 77–102 (2010).
30. G. Wu, Y. Liu, B. He, Q. Bao, A. Duan, F.-F. Jin, Thermal controls on the Asian summer monsoon. *Sci. Rep.* **2**, 404 (2012).
31. A. Zhisheng, W. Guoxiong, L. Jianping, S. Youbin, L. Yimin, Z. Weijian, C. Yanjun, D. Anmin, L. Li, M. Jiangyu, C. Hai, S. Zhengguo, T. Liangcheng, Y. Hong, A. Hong, C. Hong, F. Juan, Global monsoon dynamics and climate change. *Annu. Rev. Earth Planet. Sci.* **43**, 29–77 (2015).
32. X. Liu, J. E. Kutzbach, Z. Liu, Z. An, L. Li, The Tibetan Plateau as amplifier of orbital-scale variability of the East Asian monsoon. *Geophys. Res. Lett.* **30**, 1839 (2003).
33. R. Zhang, D. Jiang, Z. Zhang, The impact of the uplifts of the main part and marginal area of the Tibetan Plateau on the Asian monsoon climate. *Quat. Sci.* **36**, 945–952 (2016).
34. D.-Y. Yuan, W.-P. Ge, Z.-W. Chen, C.-Y. Li, Z.-C. Wang, H.-P. Zhang, P.-Z. Zhang, D.-W. Zheng, W.-J. Zheng, W. H. Craddock, K. E. Dayem, A. R. Duvall, B. G. Hough, R. O. Lease, J. D. Champagnac, D. W. Burbank, M. K. Clark, K. A. Farley, C. N. Garzione, E. Kirby, P. Molnar, G. H. Roe, The growth of northeastern Tibet and its relevance to large-scale continental geodynamics: A review of recent studies. *Tectonics* **32**, 1358–1370 (2013).
35. P. Molnar, J. M. Stock, Slowing of India's convergence with Eurasia since 20 Ma and its implications for Tibetan mantle dynamics. *Tectonics* **28**, TC3001 (2009).
36. D. Zheng, P.-Z. Zhang, J. Wan, D. Yuan, C. Li, G. Yin, G. Zhang, Z. Wang, W. Min, J. Chen, Rapid exhumation at ~8 Ma on the Liupan Shan thrust fault from apatite fission-track thermochronology: Implications for growth of the northeastern Tibetan Plateau margin. *Earth Planet. Sci. Lett.* **248**, 198–208 (2006).
37. D. Zheng, M. K. Clark, P. Zhang, W. Zheng, K. A. Farley, Erosion, fault initiation and topographic growth of the North Qilian Shan (northern Tibetan Plateau). *Geosphere* **6**, 937–941 (2010).
38. X. M. Fang, M. Yan, R. Van der Voo, D. K. Rea, C. Song, J. M. Parés, J. Gao, J. Nie, S. Dai, Late Cenozoic deformation and uplift of the NE Tibetan Plateau: Evidence from high-resolution magnetostratigraphy of the Guide Basin, Qinghai Province, China. *Geol. Soc. Am. Bull.* **117**, 1208–1225 (2005).
39. R. O. Lease, D. W. Burbank, G. E. Gehrels, Z. C. Wang, D. Y. Yuan, Signatures of mountain building: Detrital zircon U/Pb ages from northeastern Tibet. *Geology* **35**, 239–242 (2007).
40. D. K. Rea, H. Snoeckx, L. H. Joseph, Late Cenozoic eolian deposition in the North Pacific: Asian drying, Tibetan uplift, and cooling of the northern hemisphere. *Paleoceanography* **13**, 215–224 (1998).
41. Z. An, J. E. Kutzbach, W. L. Prell, S. C. Porter, Evolution of Asian monsoons and phased uplift of the Himalaya–Tibetan Plateau since Late Miocene times. *Nature* **411**, 62–66 (2001).
42. Y. Song, X. Fang, J. J. Li, Z. S. An, X. Miao, The Late Cenozoic uplift of the Liupan Shan, China. *Sci. China Ser. D* **44**, 176–184 (2001).
43. J. Nie, T. Stevens, M. Rittner, D. Stockli, E. Garzanti, M. Limonta, A. Bird, S. Andò, P. Vermeesch, J. Saylor, H. Lu, D. Breecker, X. Hu, S. Liu, A. Resentini, G. Vezzoli, W. Peng, A. Carter, S. Ji, B. Pan, Loess Plateau storage of Northeastern Tibeta Plateau-derived Yellow River sediment. *Nat. Commun.* **6**, 8511 (2015).
44. J. Nie, W. Peng, A. Möller, Y. Song, D. F. Stockli, T. Stevens, B. K. Horton, S. Liu, A. Bird, J. Oalmann, H. Gong, X. Fang, Provenance of the upper Miocene–Pliocene Red Clay deposits of the Chinese loess plateau. *Earth Planet. Sci. Lett.* **407**, 35–47 (2014).
45. T. Stevens, A. Carter, T. P. Watson, P. Vermeesch, S. Andò, A. F. Bird, H. Lu, E. Garzanti, M. A. Cottam, I. Sevastjanova, Genetic linkage between the Yellow River, the Mu Us desert, and the Chinese Loess Plateau. *Quat. Sci. Rev.* **78**, 355–368 (2013).
46. A. Licht, A. Pullen, P. Kapp, J. Abell, N. Giesler, Eolian cannibalism: Reworked loess and fluvial sediment as the main sources of the Chinese Loess Plateau. *Geol. Soc. Am. Bull.* **128**, 944–956 (2016).
47. A. Pullen, P. Kapp, A. T. McCallister, H. Chang, G. E. Gehrels, C. N. Garzione, R. V. Heermance, L. Ding, Qaidam Basin and northern Tibetan Plateau as dust sources for the Chinese Loess Plateau and paleoclimatic implications. *Geology* **39**, 1031–1034 (2011).
48. Y. Huang, S. C. Clemens, W. Liu, Y. Wang, W. L. Prell, Large-scale hydrological change drove the late Miocene C_4 plant expansion in the Himalayan foreland and Arabian Peninsula. *Geology* **35**, 531–534 (2007).
49. P. Molnar, P. England, J. Martinod, Mantle dynamics, uplift of the Tibetan Plateau, and the Indian monsoon. *Rev. Geophys.* **31**, 357–396 (1993).
50. D. A. Hodell, J. H. Curtis, F. J. Sierro, M. E. Raymo, Correlation of late Miocene to early Pliocene sequences between the Mediterranean and North Atlantic. *Paleoceanography* **16**, 164–178 (2001).
51. M. E. Raymo, W. F. Ruddiman, Tectonic forcing of late Cenozoic climate. *Nature* **359**, 117–122 (1992).
52. C. France-Lanord, L. A. Derry, Organic carbon burial forcing of the carbon cycle from Himalayan erosion. *Nature* **390**, 65–67 (1997).
53. K. E. K. St. John, L. A. Krissek, The late Miocene to Pleistocene ice-rafting history of southeast Greenland. *Boreas* **31**, 28–35 (2002).
54. A. Tzanova, T. D. Herbert, L. Peterson, Cooling Mediterranean Sea surface temperatures during the Late Miocene provide a climate context for evolutionary transitions in Africa and Eurasia. *Earth Planet. Sci. Lett.* **419**, 71–80 (2015).
55. A. Yin, Y. Q. Dang, L. Cun Wang, W. M. Jiang, S. P. Zhou, X. Hua Chen, G. E. Gehrels, M. W. McRivette, Cenozoic tectonic evolution of Qaidam basin and its surrounding regions (part 1): The southern Qilian Shan-Nan Shan thrust belt and northern Qaidam basin. *Geol. Soc. Am. Bull.* **120**, 813–846 (2008).
56. G. Dupont-Nivet, B. K. Horton, R. F. Butler, J. Wang, J. Zhou, G. L. Waanders, Paleogene clockwise tectonic rotation of the Xining-Lanzhou region, northeastern Tibetan Plateau. *J. Geophys. Res.* **109**, B04401 (2004).
57. B. K. Horton, G. Dupont-Nivet, J. Zhou, G. L. Waanders, R. F. Butler, J. Wang, Mesozoic-Cenozoic evolution of the Xining-Minhe and Dangchang basins, northeastern Tibetan Plateau: Magnetostratigraphic and biostratigraphic results. *J. Geophys. Res.* **109**, B04402 (2004).
58. M. Jolivet, M. Brunel, D. Seward, Z. Xu, J. Yang, F. Roger, P. Tapponnier, J. Malavieille, N. Arnaud, C. Wu, Mesozoic and Cenozoic tectonics of the northern edge of the Tibetan Plateau: Fission-track constraints. *Tectonophysics* **343**, 111–134 (2001).
59. K. St. John, Cenozoic ice-rafting history of the central Arctic Ocean: Terrigenous sands on the Lomonosov Ridge. *Paleoceanography* **23**, PA1S05 (2008).
60. J. S. Eldrett, I. C. Harding, P. A. Wilson, E. Butler, A. P. Roberts, Continental ice in Greenland during the Eocene and Oligocene. *Nature* **446**, 176–179 (2007).
61. L. E. Lisiecki, Links between eccentricity forcing and the 100,000-year glacial cycle. *Nat. Geosci.* **3**, 349–352 (2010).
62. P. Huybers, C. Wunsch, Obliquity pacing of the late Pleistocene glacial terminations. *Nature* **434**, 491–494 (2005).
63. Y. Sun, S. C. Clemens, Z. S. An, Z. Yu, Astronomical timescale and palaeoclimatic implication of stacked 3.6-Myr monsoon records from the Chinese Loess Plateau. *Quat. Sci. Rev.* **25**, 33–48 (2006).
64. J. Nie, J. King, X. Fang, Tibetan uplift intensified the 400 k.y. signal in paleoclimate records at 4 Ma. *Geol. Soc. Am. Bull.* **120**, 1338–1344 (2008).
65. Y. Sun, J. Chen, S. C. Clemens, Q. Liu, J. Ji, R. Tada, East Asian monsoon variability over the last seven glacial cycles recorded by a loess sequence from the northwestern Chinese Loess Plateau. *Geochem. Geophys. Geosyst.* **7**, Q12Q02 (2006).
66. P. X. Wang, The role of west Pacific marginal seas in glacial aridification of China: A preliminary study. *Quat. Sci.* **1**, 32–42 (1995).
67. A. Zhisheng, S. C. Clemens, J. Shen, X. Qiang, Z. Jin, Y. Sun, W. L. Prell, J. Luo, S. Wang, H. Xu, Y. Cai, W. Zhou, X. Liu, W. Liu, Z. Shi, L. Yan, X. Xiao, H. Chang, F. Wu, L. Ai, F. Lu, Glacial-Interglacial Indian Summer Monsoon Dynamics. *Science* **333**, 719–723 (2011).
68. S. C. Clemens, W. L. Prell, Y. Sun, Z. Liu, G. Chen, Southern Hemisphere forcing of Pliocene $\delta^{18}O$ and the evolution of Indo-Asian monsoons. *Paleoceanography* **23**, PA4210 (2008).
69. M. E. Raymo, L. E. Lisiecki, K. H. Nisancioglu, Plio-Pleistocene ice volume, Antarctic climate, and the global $\delta^{18}O$ record. *Science* **313**, 492–495 (2006).
70. H. Pälike, R. D. Norris, J. O. Herrle, P. A. Wilson, H. K. Coxall, C. H. Lear, N. J. Shackleton, A. K. Tripati, B. S. Wade, The heartbeat of the Oligocene climate system. *Science* **314**, 1894–1898 (2006).
71. D. Liebrand, L. J. Lourens, D. A. Hodell, B. de Boer, R. S. W. van de Wal, H. Pälike, Antarctic ice sheet and oceanographic response to eccentricity forcing during the early Miocene. *Clim. Past* **7**, 869–880 (2011).
72. Y. G. Zhang, M. Pagani, Z. Liu, S. M. Bohaty, R. DeConto, A 40-million-year history of atmospheric CO_2. *Philos. Trans. R. Soc. A* **371**, 20130096 (2013).
73. A. Licht, M. van Cappelle, H. A. Abels, J.-B. Ladant, J. Trabucho-Alexandre, C. France-Lanord, Y. Donnadieu, J. Vandenberghe, T. Rigaudier, C. Lécuyer, D. Terry Jr., R. Adriaens, A. Boura, Z. Guo, A. N. Soe, J. Quade, G. Dupont-Nivet, J.-J. Jaeger, Asian monsoons in a late Eocene greenhouse world. *Nature* **513**, 501–506 (2014).
74. A. Licht, G. Dupont-Nivet, A. Pullen, P. Kapp, H. A. Abels, Z. Lai, Z. Guo, J. Abell, D. Giesler, Resilience of the Asian atmospheric circulation shown by Paleogene dust provenance. *Nat. Commun.* **7**, 12390 (2016).
75. M. Huber, A. Goldner, Eocene monsoons. *J. Asian Earth Sci.* **44**, 3–23 (2012).
76. G. Dupont-Nivet, W. Krijgsman, C. G. Langereis, H. A. Abels, S. Dai, X. Fang, Tibetan Plateau aridification linked to global cooling at the Eocene–Oligocene transition. *Nature* **445**, 635–638 (2007).

77. Q. Liu, A. P. Roberts, J. Torrent, C.-S. Horng, J. C. Larrasoana, What do the HIRM and *S*-ratio really measure in environmental magnetism? *Geochem. Geophys. Geosyst.* **8**, Q09011 (2007).
78. D. Heslop, M. Dillon, Unmixing magnetic remanence curves without a priori knowledge. *Geophys. J. Int.* **170**, 556–566 (2007).
79. J. Nie, R. Zhang, C. Necula, D. Heslop, Q. Liu, L. Gong, S. Banerjee, Late Miocene–early Pleistocene paleoclimate history of the Chinese Loess Plateau revealed by remanence unmixing. *Geophys. Res. Lett.* **41**, 2163–2168 (2014).
80. D. Heslop, T. von Dobeneck, M. Höcker, Using non-negative matrix factorization in the "unmixing"of diffuse reflectance spectra. *Mar. Geol.* **241**, 63–78 (2007).
81. M. A. Bush, J. E. Saylor, B. K. Horton, J. Nie, Growth of the Qaidam Basin during Cenozoic exhumation in the northern Tibetan Plateau: Inferences from depositional patterns and multiproxy detrital provenance signatures. *Lithosphere* **8**, 58–82 (2016).
82. W. Balsam, J. Ji, J. Chen, Climatic interpretation of the Luochuan and Lingtai loess sections, China, based on changing iron oxide mineralogy and magnetic susceptibility. *Earth Planet. Sci. Lett.* **223**, 335–348 (2004).
83. P. Hu, Q. Liu, J. Torrent, V. Barrón, C. Jin, Characterizing and quantifying iron oxides in Chinese loess/paleosols: Implications for pedogenesis. *Earth Planet. Sci. Lett.* **369–370**, 271–283 (2013).
84. Y. X. Gao, On some problems of Asian monsoon, in *Some Questions about the East Asian Monsoon,* Y. X. Gao, Ed. (Chinese Science Press, 1962), pp. 1–49.
85. J. Nie, T. Stevens, Y. Song, J. W. King, R. Zhang, S. Ji, L. Gong, D. Cares, Pacific freshening drives Pliocene cooling and Asian monsoon intensification. *Sci. Rep.* **4**, 5474 (2014).
86. Z. T. Guo, W. F. Ruddiman, Q. Z. Hao, H. B. Wu, Y. S. Qiao, R. X. Zhu, S. Z. Peng, J. J. Wei, B. Y. Yuan, T. S. Liu, Onset of Asian desertification by 22 Myr ago inferred from loess deposits in China. *Nature* **416**, 159–163 (2002).
87. C. Torrence, G. P. Compo, A practical guide to wavelet analysis. *Bull. Am. Meteorol. Soc.* **79**, 61–78 (1998).
88. D. Paillard, L. Labeyrie, P. Yiou, Macintosh program performs time-series analysis. *EOS* **77**, 379 (1996).
89. J. Laskar, P. Robutel, F. Joutel, M. Gastineau, A. C. M. Correia, B. Levrard, A long-term numerical solution for the insolation quantities of the Earth. *Astron. Astrophys.* **428**, 261–285 (2004).

Acknowledgments: Constructive comments by the associate editor K. Whipple and three reviewers significantly improved the manuscript. We thank L. Gong and M. Li for laboratory assistance and Q. Meng, Y. Miao, S. Ji, W. Peng, and K. He for field assistance. **Funding:** This work was funded by the national key research and development program of China (2016YFE0109500), the (973) National Basic Research Program of China (grant no. 2013CB956400), the Strategic Priority Research Program of the Chinese Academy of Sciences (grant no. XDB03020400), the National Natural Science Foundation of China (grant nos. 41422204, 41172329, and 41290253), and the U.S. NSF (grant no. 1545859). **Author contributions:** J.N. and Q.L. designed the experiments. Q.S., R.Z., C.N., and Z.L. performed the experiments. All authors analyzed the data. J.N. wrote the manuscript with help from the other authors. **Competing interests:** The authors declare that they have no competing interests. **Data and materials availability:** All data needed to evaluate the conclusions in the paper are present in the paper and/or the Supplementary Materials. Additional data related to this paper may be requested from the authors.

Submitted 10 April 2016
Accepted 10 February 2017
Published 29 March 2017
10.1126/sciadv.1600762

Citation: J. Nie, C. Garzione, Q. Su, Q. Liu, R. Zhang, D. Heslop, C. Necula, S. Zhang, Y. Song, Z. Luo, Dominant 100,000-year precipitation cyclicity in a late Miocene lake from northeast Tibet. *Sci. Adv.* **3**, e1600762 (2017).